OPEN

Anatomy of a microearthquake sequence on an active normal fault

T. A. Stabile[1,3], C. Satriano[1,2], A. Orefice[1], G. Festa[1] & A. Zollo[1]

[1]Dipartimento di Scienze Fisiche, Università di Napoli Federico II, Naples, Italy, [2]Institut de Physique du Globe de Paris, Paris, France, [3]Istituto di Metodologie per l'Analisi Ambientale, CNR-IMAA, Tito (PZ), Italy.

Correspondence and
requests for materials
should be addressed to
T.A.S. (tony.stabile@
imaa.cnr.it)

The analysis of similar earthquakes, such as events in a seismic sequence, is an effective tool with which to monitor and study source processes and to understand the mechanical and dynamic states of active fault systems. We are observing seismicity that is primarily concentrated in very limited regions along the 1980 Irpinia earthquake fault zone in Southern Italy, which is a complex system characterised by extensional stress regime. These zones of weakness produce repeated earthquakes and swarm-like microearthquake sequences, which are concentrated in a few specific zones of the fault system. In this study, we focused on a sequence that occurred along the main fault segment of the 1980 Irpinia earthquake to understand its characteristics and its relation to the loading-unloading mechanisms of the fault system.

Observing and studying the seismicity of active faults has proven to be a fundamental step in studying the geometry, mechanical properties, and time-dependent processes of fault zones. The accurate relocation and study of the source properties of large catalogues of earthquakes were used to produce high-resolution images of complex fault systems (e.g.[1]); characterise the small-scale variability of faulting style, stress and strength (e.g.[2]); test mechanical models of rupture (e.g.[3]); and study the processes associated with the triggering of earthquakes and earthquake migration (e.g.[4]).

Within this framework, repeated earthquakes are found to exhibit unique characteristics. For example, seismic sequences that occur within a very small source area are characterised by highly similar waveforms[5,6]. These events offer a unique opportunity to study the fault processes at time scales that range from hours to years. These similar earthquakes can be located with great precision and can provide accurate estimates of the local stress regime, the mechanical properties of the fault, and the efficiency of the loading mechanism[7,8].

The goal of observing the seismicity of an active fault system during its inter-seismic period has led to the development of a dense seismic network (ISNet - Irpinia Seismic Network) that has been operational since 2005 in Southern Italy along the Campania-Lucania Apennine [9]. ISNet includes a complete catalogue of events since 2008 and constitutes a unique field laboratory, which monitors and studies the source processes in a complex seismo-genic region that is characterised by prevalent normal-faulting seismicity and is capable of generating earthquakes up to magnitude 7. The most recent of these high-magnitude earthquakes was the M 6.9 Irpinia earthquake in 1980[10]. This was a complex, normal-faulting event characterised by different rupture episodes that nucleated along three different fault segments, with a total approximate length of 60 km. The projections of those fault segments are shown in Figure 1. This earthquake was the first in Italian history to produce substantial and clear surface faulting. Westaway and Jackson[11] were the first to discover more than 10 km of breakage surface faulting. Based on their field work, Pantosti and Valensise[12] subsequently reconstructed three main strands, which together formed a 38-km-long, northwest-trending fault scarp.

Since 2008, ISNet has recorded approximately 1,200 events along the Campania-Lucania Apennines, each with a local magnitude (ML) of less than 3.4[13]. All of the data were acquired with a sampling frequency of 125 Hz. The majority of the recorded seismicity is concentrated in a small number of regions along the 1980 Irpinia earthquake fault zone. These zones of weakness produce repeated earthquakes and swarm-like microearthquake sequences (Figure 1) that last from 2 to 5 days. They have a maximum moment magnitude of less than 3 and are char-acterised by co-located events that share the same focal mechanism, which has been observed in the area[14]. Supplementary Figure S1 demonstrates that these observations are not related to the ISNet geometry because the zones of weakness still remain when the seismicity is considered over the complete location threshold of the network (ML = 1.3)[14].

In this paper, we describe the steps of the detailed analysis that we performed on one of the sequences. We discuss our results to enable a better understanding of the processes that control the occurrence and size of
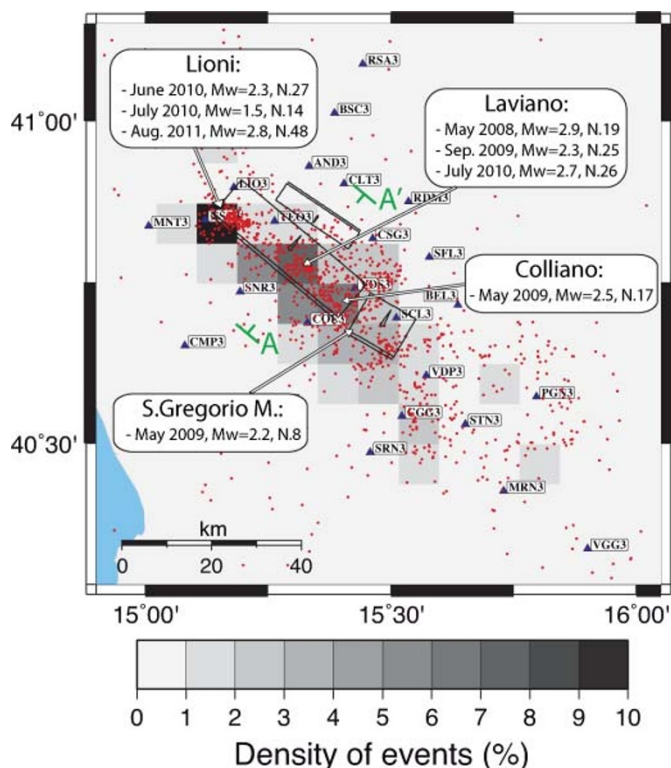
Figure 1 | Density map of the 1200 microearthquakes located by the ISNet since 2008. The events are displayed on the map with red circles. The seismicity is concentrated in very limited regions along the 1980 Irpinia earthquake fault zone, where the majority of the recorded sequences occurred. AA' indicates the vertical cross section reported in Figure 6.

microearthquakes in a single swarm and the relation of these processes to the fault system loading-unloading mechanisms.

Results

The analysed microearthquake sequence occurred in May 2008 and lasted for 3 days. The sequence consisted of 19 small earthquakes

(0.8 < Mw < 2.9), which were located near the village of Laviano. The sequence was recorded by 21 stations in the ISNet network and 11 stations in the Italian National Institute of Geophysics and Volcanology (INGV) network, thus providing a total number of 242 P-wave picks and 165 S-wave picks. The striking waveform similarity and the clarity of the P-wave first motion polarity at different stations indicated that events were co-located and shared the same focal mechanism. An example of the strong similarity between each event is shown in Figure 2. This figure shows band-pass-filtered (1–20 Hz), normalised waveforms of the velocimetric vertical-component records at the COL3, SNR3, and VDS3 stations for all of the microearthquakes in the sequence. For the main event, we also measured 26 P-wave first motion polarities.

The absolute location of the sequence indicates that the events occurred within errors along the main fault segment of the 1980 Irpinia earthquake, at an average depth of 10 km. After the double-difference relocation process (see the Methods section), we found that the events in the sequence were highly concentrated to a volume of less than 300 m per side and were clearly aligned along an approximately E-W direction, with the fault strike (287°) of the main event shown in Figure 3a. Regarding the relative location, the estimated average vertical error was of approximately 80 meters, while the estimated average horizontal error was of approximately 20 m (Supplementary Table S1). Although the events were extremely similar among the different stations, which are shown in Figure 2, small differences within a few samples in Ts-Tp times between pairs of microearthquakes were allowed to resolve small variations in the event locations. Windows of 0.5 seconds around the S-wave arrival time at the north component of the SNR3 and COL3 stations are reported in Figure 3c and Figure 3d, respectively. In these figures, traces of each event are aligned with respect to the first P-wave arrival, and the main event (event 12) is indicated with a red line. While a difference is not evident at the COL3 station, it can be seen that at the SNR3 station, the S-wave for some events, including the main event, arrived in advance compared to the rest of the S-waves in the sequence. These observations were consistent with a location of those events nearest to the SNR3 station, as shown in Figure 3(a and b).

The sequence started on May 25, 2008, with an event of magnitude Mw = 1.0 at 2:53 UTC. During that day, ten microearthquakes occurred, with moment magnitudes ranging from 0.8 to 1.5. On May 26, only one event occurred. At 16:19 UTC on May 27, the main event (Mw = 2.9) occurred west of the area affected by
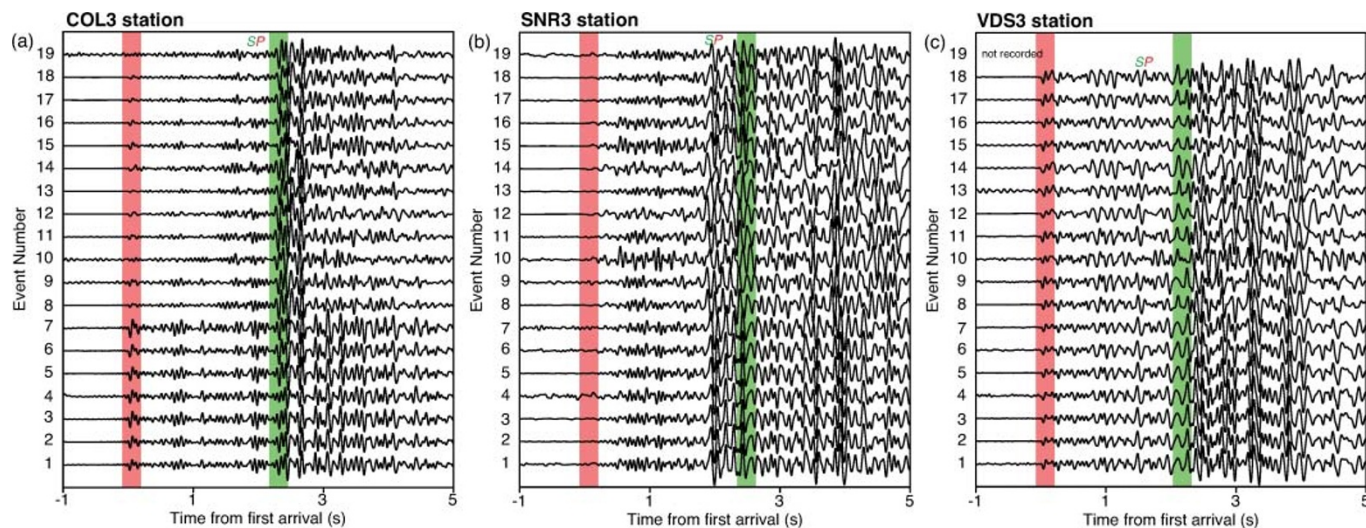

Figure 2 | Vertical-component velocity records of the seismic sequence at the (a) COL3, (b) SNR3, and (c) VDS3 stations. The waveforms are band-pass-filtered from 1 to 20 Hz and are amplitude-normalised. Events are ordered in time from earliest to latest and the event number increases with the event origin time. Waveforms are aligned with respect to the first P-wave arrival time. Red and green vertical bars indicate windows containing the P- and S-wave arrival times, respectively. The S-to-P (SP) conversion at shallow interfaces is also indicated.
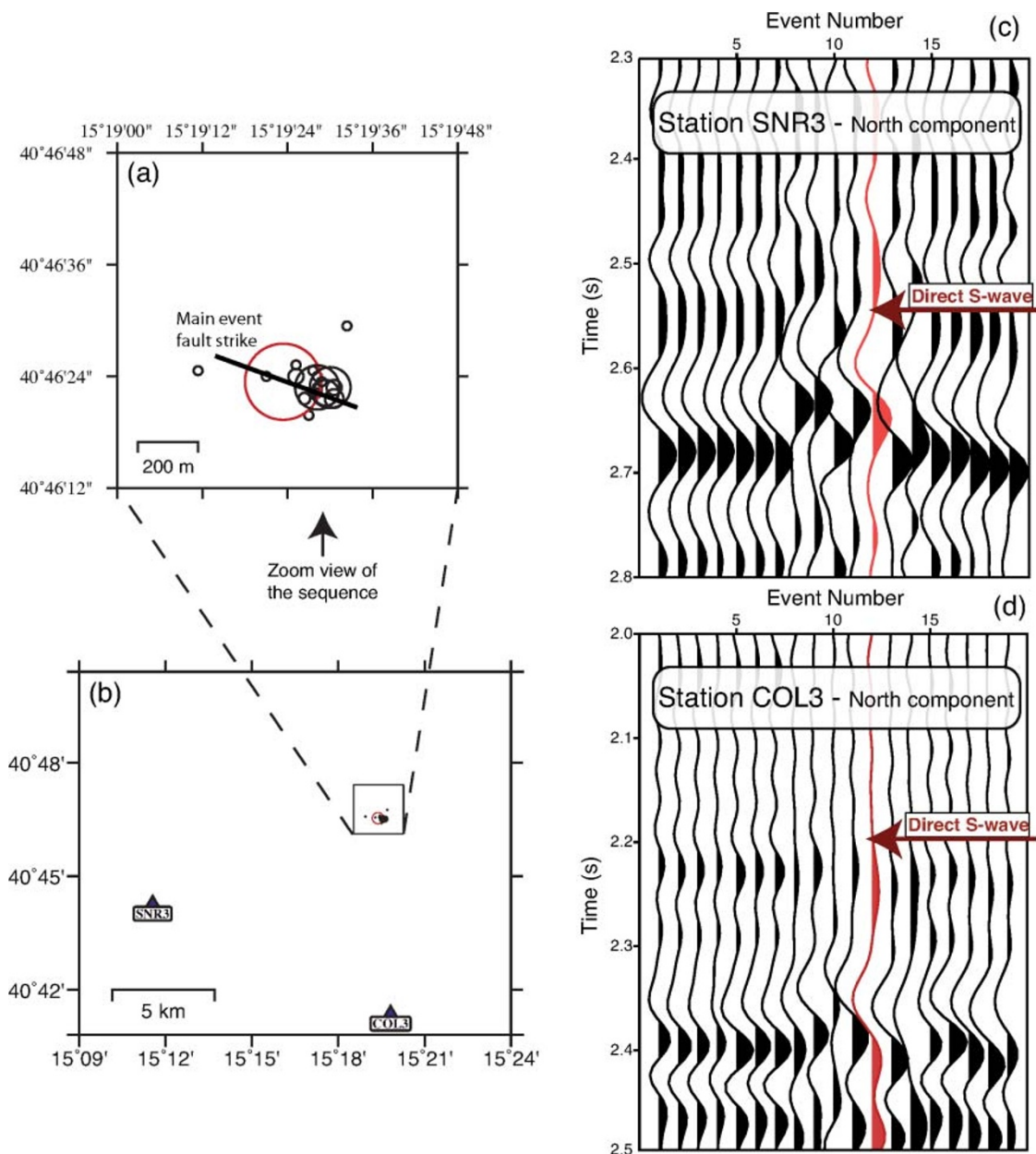
Figure 3 | (a) Epicentres of the analysed seismic sequence. The fault strike ($287°$) of the main event is indicated with a black line crossing the rupture area of the main event (red circle). (b) Relative position of the sequence with respect to the SNR3 and COL3 stations. (c, d) Record of the north component of the SNR3 and COL3 stations in a 0.5-second window around the S-wave arrival time. The traces of each event are aligned with respect to the first P-wave arrival, and the main event (event 12) is indicated with a red colour. The main differences in S-wave arrival times are demonstrated at the SNR3 station.

microearthquakes during the previous two days. Subsequently, the region in which the other events occurred was activated again by six microearthquakes until May 28, with moment magnitudes ranging from 1.6 to 2.3. The last event of magnitude 1.2 occurred to the west of the main event at a distance of approximately 200 m. The progression of the sequence in time is shown in the Supplementary Figure S2.

The main event of the sequence (Mw = 2.9) was clearly the largest event, as its seismic moment ($2.4×10^{13}$ Nm) was approximately 2.5 times larger than the cumulative seismic moment of the other microearthquakes ($9.9×10^{12}$ Nm, corresponding to Mw = 2.6).

After assuming circular crack rupture propagation, we estimated the source radius and the stress drop from the inversion of the S-wave displacement spectra (see the Methods section). We found that the high-frequency decay of the S-wave displacement spectra was proportional to $ω^{-γ}$, with $γ = 1.51 ± 0.68$. A self-similar scaling law was

maintained, with a constant stress drop $Δσ = 3.9 ± 2.2$ MPa, as shown by the red circles in Figure 4. The constant stress drop scaling model results are appropriate after considering the entire seismicity pattern recorded by the ISNet, as represented by the grey circles in Figure 4 that span the moment range between 10^{11} and 10^{14} Nm. The self-similar, constant stress drop scaling was verified by a $χ^2$ test, which included uncertainties in the single estimates. We found that the source radius ranges from approximately 20 to 100 m. For comparison, we completed the plots by assigning each event for which there was no reliable estimation of the source radius a constant value of 17 m, which is the minimum space scale that is resolvable in this analysis. After comparing the cumulative rupture area of the smallest events to the area of the main event, the two areas were found to have approximately the same dimensions; therefore, the seismic moment of the main event is 2.5 times larger than the
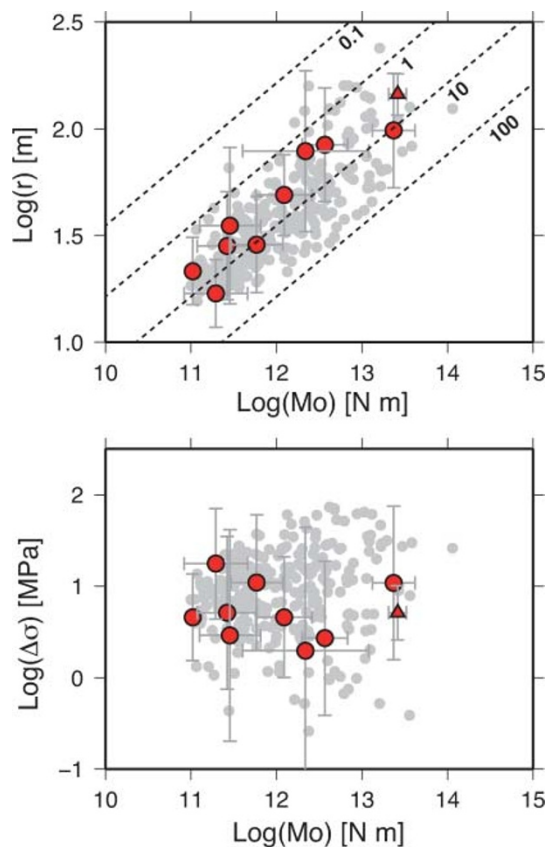
Figure 4 | Log of the source radius r (a) and the static stress drop Δσ (b) compared with the log of the seismic moment Mo. In the panel (a), dashed lines correspond to constant static stress drop values, which are expressed in MPa. Uncertainties in source parameters are reported in each panel for the events belonging to the analysed sequence (red circles). A red triangle symbol in both panels indicates the calculated estimation from the STF durations. Grey circles represent source parameter estimations for the entire catalogue of seismic events recorded by the ISNet.

cumulative seismic moment of the other events due to a greater slip. In fact, the estimated average slip ranges from 0.2 to 0.7 cm for all of the secondary events, while the value for the main event is 2.4 cm. The estimated source parameters for the entire sequence are reported in the Supplementary Table S2.

We considered the estimations of the source radius and the static stress drop for the main event obtained using the duration of the source time functions (STFs), which are the values shown in grey in the Supplementary Table S2 and displayed with triangle symbols in Figure 4. The values matched (see Figure 4) those obtained by inverting the S-displacement spectra but were more robust and showed smaller errors. The 26 P-wave first motion polarities were used with the FPFIT code[15] (see also the Methods section) to obtain the fault plane solutions of the main event. The resulting focal mechanism is reported in Figure 5a and indicates an almost pure normal faulting event. The average errors of the maximum likelihood solutions were also computed with the FPFIT code and are 4, 2, and 5° for strike, dip, and rake, respectively. Moreover, the accuracy of the solutions is also supported by a very low misfit of 0.04 and a station distribution ratio (STDR) of greater than 0.5 (see Figure 5a). We investigated which of the two nodal planes is more likely to accommodate the rupture of the main event using the isochrone back-projection technique[16]. For each plane and a fixed constant rupture velocity, we retrieved the best solution for the slip by minimising the L1 distance between the observed STFs and their synthetic estimations, which is an appropriate cost function for reproducing both the amplitude and the

shape of the STFs. By repeating the process for different rupture velocities within the range of 2.2−3.0 km/s, the minimum cost function was obtained for a rupture with a velocity of 2.3 km/s along the nodal plane with a strike of 287° and a dip of 38°. The results are shown in Figure 5b. To determine the sensitivity of the solution to the nodal plane and the rupture velocity, the vertical axis of the figure shows the normalised variation of the cost function with respect to the minimum value. After inspecting the curves, we found that the nodal plane generating the rupture is highly constrained; however, variation of the cost function with the rupture velocity is exceptionally small, thus indicating a large parameter uncertainty. The best solution for the slip distribution is shown in Figure 5c. The main event was primarily a circular crack with a slip concentration in the up-dip and positive strike directions, thus providing evidence for a possible directivity effect in those directions.

Discussion

We investigated an earthquake sequence located along the main segment of the Irpinia fault system, at an approximate 10 km depth, using the analysis of high-quality seismic data from ISNet.

We found that a self-similar source scaling relationship holds for microearthquakes of the analysed sequence, with a nearly constant static stress drop of Δσ = 3.9 ± 2.2 MPa. The hypothesis of a self-similar constant stress drop scaling was statistically verified. This value is consistent with the estimation of Δσ = 3.5 MPa for the Ms 6.9, 1980 Irpinia earthquake[17], thereby suggesting that self-similarity could extend over an extensive seismic moment range (10^{11}–10^{19} Nm) for earthquakes occurring along the Irpinia fault system. Although the stress drop is only a measure of the difference between the initial and final stress on a fault, the value obtained for this sequence suggests a similar stress loading-unloading mechanisms across several space scales along this segmented normal fault system in the Southern Apennines.

A detailed analysis of the main event waveforms revealed a kinematic complexity of the rupture at a fracture scale of a few hundred metres. The apparent source time function (Supplementary Figure S3), obtained by empirical Green's function (EGF) deconvolution at 12 stations, revealed a bi-modal time function with a generally narrower second peak, which was larger than the first peak. We associated this shape with a two-stage rupture model, which is characterised by a smooth initial nucleation and a later phase associated with a localised and relatively high-slip patch. Because the relative weight of the second stage of the rupture is large (i.e., the second peak of the STF), the spectral signature of this complex rupture results in two corner frequencies, the smaller of which is associated with the entire duration of the rupture and the larger of which is associated with the later phase. It is important to note that estimations of the corner frequency from the displacement spectra of microearthquakes may be biased by small-scale source and/or propagation effects; however, the waveform deconvolution is a more robust technique for estimating the correct source size when properly selecting the P/S wave time windows[18]. We mapped the final slip distribution on the fault plane using a back-projection technique applied to STF amplitudes. The final image revealed complexity in the slip pattern, with small values in the rupture nucleation area and a larger slip at the crack boundary. The highest values were found in the up-dip direction, west of the nucleation point. The size of the main rupture is poorly constrained because the rupture velocity is not determined by the back-projection method. However, after assuming a constant rupture velocity, the size of the high slip patch was found to be 4 to 5 times smaller than the initial, low-slip phase of the rupture. This observation is similar to what was inferred for moderate to large earthquakes, in which the largest slip values are generally localised in small-sized patches far from the rupture nucleation zone[19]. However, due to the non-uniqueness of the kinematic model, a large-amplitude, late-wave radiation can also be attributed to a sharp
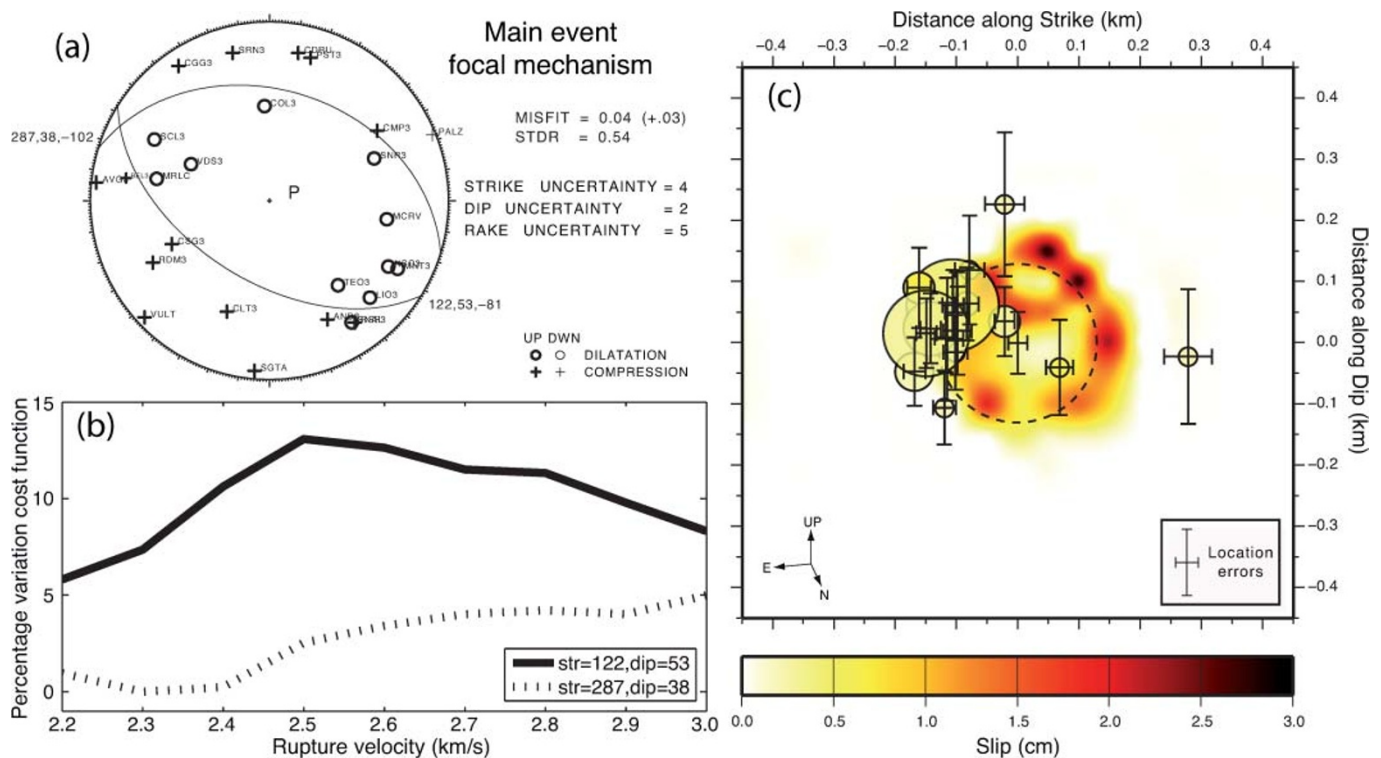
Figure 5 | (a) Fault plane solutions of the main event computed using 26 P-wave first motion polarities. P and T denote the P- and T-axis positions. Open circles and crosses indicate dilations and compressions, respectively. (b) Percentage variation of the normalised cost functions compared with the rupture velocity for both of the nodal planes. The absolute minimum was obtained for the nodal plane with a strike of 287°, a dip of 38°, and a rupture velocity of 2.3 km/s. (c) Slip map of the main event and a superimposed distribution of all microearthquakes in the sequence along the strike-dip plane. The dimensions of the circles correspond to the Madariaga's circular rupture area of the events, inferred from corner frequencies, while the colour of the circles indicates the computed average slip, Δu. Events in the sequence for which there was no reliable estimation of the source radius complete the plot by taking the minimum value estimated for that parameter. Dotted circles at the centre represent the rupture area of the main event, which was estimated using the STF durations. Horizontal and vertical location errors are also displayed.

increase of the slip rate and/or the rupture velocity at the crack border.

The smaller-magnitude events in the sequence were primarily located east of the main event rupture surface. When looking at their locations, projected on the main event fault plane (Figure 5c), their rupture surfaces nearly overlap. This indicates that the mechanism of static stress transfer is likely responsible for controlling the time progression of the sequence. The cumulative rupture area of the smaller-magnitude events is the same as that of the main event, while the cumulative seismic moment of smaller-sized earthquakes is 2.5 times less than the seismic moment of the main event; therefore, this difference results in the highest average slip.

The focal mechanisms of each event and the directivity analysis for the main event reveal a clear, normal fault mechanism occurring along a plane plunging northeast at 38° angle. This angle is less steep than the 60° fault dip estimated for the Ms 6.9, 1980 Irpinia earthquake from first motion polarities of regional data[11] (references therein). The surface projection of a 38° dipping plane crossing the sequence area is 8.5 km far away from the fault scarp of the 1980 earthquake, which is instead compatible with a 60° dipping plane (Figure 6). This may indicate a possible fault dip change between the shallow and deep portions or an abrupt slope change related to a kink, a branch or a fork near 10 km depth. The presence of a fault kink or bend at a depth of approximately 10 km was also hypothesised by Westaway and Jackson[11] to explain the later phases of the main rupture of the Irpinia earthquake on the basis of vertical ground levelling data and aftershock distribution.

Listric or kinked fault geometries are not unusual in normal faulting tectonic contexts[20]. The anomalously large stress concentration

may be the cause of the generation of small fractures near the zone where the fault slope changes, which are likely to cause the fault zone to be strongly damaged and/or fractured. This zone could be the source of repeated earthquake activity due to the internal mechanical re-adjustments from local stress release and/or fluid migration along the fault zone near the geometrical barrier. Such seismic movements can produce a crackling noise, which also occurs due to other phenomena such as sound emission during paper crumpling, fluids
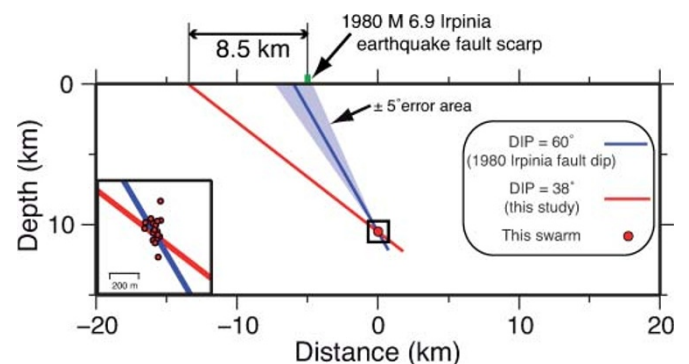

Figure 6 | **Sketch of the fault planes projected on the AA' vertical cross section (see Figure 1).** The red line corresponds to the fault plane obtained in this study, while the blue line corresponds to the main segment of the 1980 Irpinia earthquake. The inset in the left corner shows a close-up image of the analysed microearthquake sequence.

invading porous material, solar flares, Barkhausen noise and fractures in heterogeneous material[21].

Overcoming a geometrical barrier for an earthquake is not as easy as moving along a planar surface. In addition, the probability for a rupture to turn around a bend depends on the orientation of the bend itself, the bend angle, the remote stress orientation and the local rupture velocity. Furthermore, it depends on which of the two branches the rupture nucleates. With a vertical principal stress, σ_1, and a horizontal principal stress, σ_3, the stress drop is nearly the same along the two segments, and is almost independent of the ratio σ_1/σ_3 and the dynamic friction, indicating that the two segments have the same ability to sustain a propagating rupture. However, a rupture developing along the steeper part of the fault is not dynamically favoured over down-dip propagation and turning around the bend[22,23]. Additionally, occurrence of swarm-like sequences on the compressional side of the kink reduces the normal stress on the steeper portion of the fault, increasing the probability for the nucleation of large events along this latter side of the fault[24]. This could have been the case of the 1980 Irpinia earthquake that nucleated at a depth of approximately 10 km along the steep portion of the fault and propagated up-dip until it broke the free surface. Hence, monitoring seismic sequences and separating physical processes that occur after seismic events may help to define seismicity rates along the fault system and the probability of moderate-to-large-magnitude (M>6) earthquake occurrences.

Methods

We initially identified the accurate absolute locations of the events using a nonlinear global approach (NonLinLoc)[25] in a 3-D velocity model of the Campania-Lucania area[26,27]. Subsequently, we refined the locations by applying a double-difference technique (HypoDD)[28], which solves the double-difference equations using the singular value decomposition, in the equivalent layer-averaged 1-D velocity model[29]. This second step allowed for the minimisation of error due to un-modelled velocity structures because ray paths from the events to a common station are similar; in fact, hypocentral separations among earthquakes in the swarm are small compared to the event-station distance and the length scale of the velocity heterogeneities. We used both accurate manual picks and cross-correlation differential travel-times of P- and S-waves in the earthquake relocation procedure. The cross-correlation differential travel-times were computed in the frequency domain using the CCHAR program[30], resulting in a dataset of 3,906 differential times. Prior to cross-correlation, the CCHAR code performed adaptive waveform pre-filtering, which was based on cross-coherency. This filtering assigned lower weights to incoherent frequency bands while reducing the risk of the removal of potentially useful signals by the *a priori* band-pass filter choice. In particular, our CC analyses used a window length of 125 (150) samples, at 1 (1.2) second each, with a pre-pick offset of 0.2 (0.4) seconds for the P-wave (S-wave) picks. Since the waveform cross-correlation data included differential times of higher accuracy than the individual picks[31,32], their use in the double-difference algorithm gave accurate relative event relocations[8,28,33]. Double-difference relocations for events in the sequence are shown in Supplementary Table S1 with their respective uncertainties.

After assuming a source model with a high-frequency decay proportional to $\omega^{-\gamma}$ (γ is an inverted parameter), refined estimations of the spectral amplitude Ω_o and the corner frequency ω_c were obtained by inverting the observed S-wave displacement spectra in the frequency range of 0.5–50 Hz. Following an inversion strategy similar to that used by De Lorenzo et al.[34], we adopted a multi-step, non-linear, iterative procedure aimed at the joint determination of the source, the medium attenuation parameters along with a frequency-dependent parameter, and the site amplification function[35]. Specifically, we applied the non-linear Levenberg-Marquardt least-squares algorithm[36], which was implemented in the software package GNUPLOT[37], for curve-fitting and parameter estimation. In the curve-fitting, the signal-to-noise ratio was calculated in the entire range of frequencies and was used as a weighting factor; the noise level was calculated from a time window of 2.5 seconds before the first P-wave arrival. With respect to the spectral analysis, the S-wave displacement spectrum was calculated as the modulus of the two horizontal-component spectra in a time window of 2.5 s, which started 0.25 s before the S-wave onset and ended 2.25 s after the onset. The use of a small time window around the direct S-wave arrivals reduces the influence from common propagation effects that can affect the resulting parameters[38].

Starting from the estimates of the spectral parameters Ω_o and ω_c, we calculated the seismic moment M_o[39] and the source radius r[40] for nine microearthquakes recorded by at least three stations and with signal-to-noise ratios larger than two throughout the entire frequency range. The seismic moment and the radius of circular fault ruptures were then used to estimate the static stress drop $\Delta\sigma$[41] and the average slip Δu[39].

We studied the rupture process of the largest magnitude event by first determining its focal mechanism with the FPFIT code[15], which uses the information provided by P-wave first motion polarities, and after by performing a kinematic rupture modelling through the deconvolution of the empirical Green's function (EGF). In particular, the inversion of the FPFIT code was accomplished through a grid search step of one degree. With regard to the kinematic rupture modelling, to retrieve a reliable apparent source time function (STF), we first applied the stabilised deconvolution technique of Vallée[42], in which causality, positivity, limited duration and equal area constraints on the STF are integrated in the deconvolution process. The Mw = 1.9 microearthquake that occurred on 2008-5-27 at 17:25 UTC was used as the EGF; in fact, it was among the smallest of the events and it was recorded by a large number of stations. We then estimated the STF at 12 recording stations (Supplementary Figure S3) in the S-wave time window. We finally performed a kinematic rupture inversion using the isochrone back-projection technique[16]. The inversion of STFs allowed us to constrain the fault plane and provided us with an estimation of the slip distribution, rupture direction, and average velocity.

After using the STF durations, additional estimations of the corner frequency, the source radius, and the static stress drop were obtained. The values are reported in the Supplementary Table S2 and are plotted in Figure 4 with triangle symbols.

1. Waldhauser, F. & Schaff, D. P. Large-scale relocation of two decades of Northern California seismicity using cross-correlation and double-difference methods. *J. Geophys. Res.* **113**, B08311 (2008).
2. Hardebeck, J. L. Homogeneity of small-scale earthquake faulting, stress, and fault strength. *Bull. Seismol. Soc. Am.* **96**(5), 1675–1688 (2006).
3. Zaliapin, I. & Ben-Zion, Y. Asymmetric distribution of aftershocks on large faults in California. *Geophys. J. Int.* **185**(3), 1288–1304 (2011).
4. King, G. & Cocco, M. Fault interaction by elastic stress changes: New clues from earthquake sequences. *Advances in Geophysics* **44**, 1-38 (2001).
5. Nadeau, R. M. & McEvilly, T. V. Fault slip rates at depth from recurrence intervals of repeating microearthquakes. *Science* **285**(5428), 718 (1999).
6. Nadeau, R. M. & McEvilly, T. V. Periodic pulsing of characteristic microearthquakes on the San Andreas Fault. *Science* **303**(5655), 220 (2004).
7. Vidale, J., Ellsworth, W. L., Cole, A. & Marone, C. Variations in rupture process with recurrence interval in a repeated small earthquake. *Nature* **368**(6472), 624–626 (1994).
8. Waldhauser, F. & Ellsworth, W. L. Fault structure and mechanics of the Hayward Fault, California, from double-difference earthquake locations. *J. Geophys. Res.* **107**, B3 (2002).
9. Iannaccone, G. *et al.* A prototype system for earthquake early-warning and alert management in southern Italy. *Bull. Earthq. Eng.* **8**(6), 1105–1129 (2010).
10. Bernard, P. & Zollo, A. The Irpinia (Italy) 1980 earthquake: detailed analysis of a complex normal fault. *J. Geophys. Res.* **94**, 1631–1647 (1989).
11. Westaway, R. W. C. & Jackson, J. The earthquake of 1980 November 23 in Campania-Basilicata (southern Italy). *Geophys. J. R. Astr. Soc.* **90**, 375–443 (1987).
12. Pantosti, D. & Valensise, G. Faulting mechanism and complexity of the November 23, 1980, Campania-Lucania earthquake, inferred from surface observations. *J. Geophys. Res.* **95**(B10), 15319–15341 (1990).
13. Bobbio, A., Vassallo, M. & Festa, G. A local magnitude scale for Southern Italy. *Bull. Seismol. Soc. Am.* **99**, 2461–2470 (2009).
14. De Matteis, R. *et al.* Analysis of background microseismicity for crustal velocity model, fault delineation and regional stress direction in Southern Apennines, Italy. *Bull. Seismol. Soc. Am.* **102**(4), in press (2012).
15. Reasenberg, P. & Oppenheimer, D. FPFIT, FPPLOT and FPPAGE: Fortran computer programs for calculating and displaying earthquake fault plane solutions. *U.S. Geol. Surv., Open File Report* 85–739 (1985).
16. Festa, G. & Zollo, A. Fault slip and rupture velocity inversion by isochrone backprojection. *Geophys. J. Int.* **166**(2), 745–756 (2006).
17. Deschamps, A. & King, G. C. P. The Campania-Lucania (southern Italy) earthquake of 23 November 1980. *Earth Planet. Sci. Lett.* **62**, 296–304 (1983).
18. Viegas, G., Abercrombie, R. E. & Kim, W.-Y. The 2002 M5 Au Sable Forks, NY, earthquake sequence: Source scaling relationships and energy budget. *J. Geophys. Res.* **115**, B07310 (2010).
19. Mai, P. M., Spudich, P. & Boatwright, J. Hypocenter locations in finite-source rupture models. *Bull. Seismol. Soc. Am.* **95**, 965–980 (2005).
20. Eyidogan, H. & Jackson, J. A. A seismological study of normal faulting in the Demirci, Alasehir and Gediz earthquakes of 1969-1970 in western Turkey: implications for the nature and geometry of deformation in the continental crust. *Geophys. J. R. Astr. Soc.* **81**, 569–607 (1985).
21. Sethna, J. P., Dahmen, K. A. & Myers, C. R. Crackling noise. *Nature* **410**(6825), 242–250 (2001).
22. Kame, N., Rice, J. R. & Dmowska, R. Effects of pre-stress state and rupture velocity on dynamic fault branching. *J. Geophys. Res.* **108**(B5), 2265 (2003).
23. Festa, G. & Vilotte, J.-P. Role of the fault geometry on the rupture dynamics and the radiated wavefield. *AGU Fall Meeting*, S54C-05, San Francisco, USA, 5–9 December (2011).
24. Duan, B. & Oglesby, D. D. The dynamics of thrust and normal faults over multiple earthquake cycles: Effects of dipping fault geometry. *Bull. Seismol. Soc. Am.* **95**(5), 1623–1636 (2005).
25. Lomax, A., Virieux, J., Volant, P. & Berge, C. Probabilistic earthquake location in 3D and layered models: Introduction of a Metropolis-Gibbs method and comparison with linear locations. in *Advances in Seismic Event Location*, Thurber, C. H. & Rabinowitz, N. (eds.), Kluwer, Amsterdam, 101–134 (2000).

26. De Matteis, R., Romeo, A., Pasquale, G., Iannaccone, G. & Zollo A. 3D tomographic imaging of the southern Apennines (Italy): A statistical approach to estimate the model uncertainty and resolution. *Studia Geophysica et Geodaetica* **54**(3), 367–387 (2010).

27. Matrullo, E., Amoroso, O., De Matteis, R., Satriano, C. & Zollo A. 1D versus 3D velocity models for earthquake locations: a case study in Campania-Lucania region (Southern Italy). *EGU General Assembly*, EGU2011-9305, Vienna, Austria, 3–8 April (2011).

28. Waldhauser, F. & Ellsworth, W. L. A double-difference earthquake location algorithm: Method and application to the northern Hayward Fault, California. *Bull. Seismol. Soc. Am.* **90**, 1353–1368 (2000).

29. Lin, G., Shearer, P. M. & Hauksson, E. Applying a three-dimensional velocity model, waveform cross correlation, and cluster analysis to locate southern California seismicity from 1981 to 2005. *J. Geophys. Res.* **112**, B12309 (2007).

30. Rowe, C. A., Aster, R. C., Borchers, B. & Young, C. J. An automatic, adaptive algorithm for refining phase picks in large seismic data sets. *Bull. Seismol. Soc. Am.* **92**(5), 1660–1674 (2002).

31. Poupinet, G., Ellsworth, W. L. & Frechet, J. Monitoring velocity variations in the crust using earthquake doublets: An application to the Calaveras Fault, California. *J. Geophys. Res.* **89**, 571–5731 (1984).

32. Shearer, P. M. Evidence from a cluster of small earthquakes for a fault at 18 km depth beneath Oak Ridge, southern California. *Bull. Seismol. Soc. Am.* **88**, 1327–1336 (1998).

33. Hauksson, E. & Shearer, P. M. Southern California hypocenter relocation with waveform cross-correlation, part 1: Results using the double- difference method. *Bull. Seismol. Soc. Am.* **95**, 896–903 (2005).

34. De Lorenzo, S., Zollo, A. & Zito, G. Source, attenuation, and site parameters of the 1997 Umbria-Marche seismic sequence from the inversion of P wave spectra: A comparison between constant Qp and frequency-dependent Qp models. *J. Geophys. Res.* **115**, B09306 (2010).

35. Zollo, A., Orefice, A. & Convertito, V. Scaling relationships for earthquake source parameters down to decametric fracture lengths. *EGU General Assembly*, EGU2011-6608, Vienna, Austria, 3–8 April (2011).

36. Marquardt, D. An algorithm for least-squares estimation of nonlinear parameters, SIAM. *J. Appl. Math.* **11**, 431–441 (1963).

37. Janert, K. P. *Gnuplot in Action: Understanding Data with Graphs.* Manning Publications Co. 396 pp. (2009).

38. Ide, S., Beroza, G., Prejean, S. & Ellsworth, W. Apparent break in earthquake scaling due to path and site effects on deep borehole recordings. *J. Geophys. Res.* **108**(B5), 2271 (2003).

39. Aki, K. & Richards, P. G. *Quantitative Seismology (2nd edition)*. University Science Books 704 pp. (2002).

40. Madariaga, R. Dynamics of an expanding circular fault. *Bull. Seismol. Soc. Am.* **66**, 639–666 (1976).

41. Keilis-Borok, V. I. On the estimation of the displacement in an earthquake source and of source dimensions. *Ann. Geophys.* **12**, 205–214 (1959).

42. Vallée, M. Stabilizing the empirical Green function analysis: development of the projected Landweber method. *Bull. Seismol. Soc. Am.* **94**, 394–409 (2004).

Author contributions

T.A.S. and C.S. contributed with the earthquake location. A.O. and A.Z. computed the source parameters and the STFs. T.A.S. determined the focal mechanism. G.F. performed the kinematic rupture inversion. All authors contributed to write the manuscript and to discuss the results.

Additional information

Supplementary information accompanies this paper at http://www.nature.com/scientificreports

Competing financial interests: The authors declare no competing financial interests

How to cite this article: Stabile, T.A., Satriano, C., Orefice, A., Festa, G. & Zollo, A. Anatomy of a microearthquake sequence on an active normal fault. *Sci. Rep.* **2**, 410; DOI:10.1038/srep00410 (2012).